Analyzing the microstructure of cemented fills adding polypropylene-glass fibers with X-ray micro-computed tomography

Jiajian Li [a,b,***], Shuai Cao [a,b,*], Erol Yilmaz [c,**]

[a] State Key Laboratory of High-Efficient Mining and Safety of Metal Mines of Ministry of Education, University of Science and Technology Beijing, Beijing 100083, China
[b] School of Civil and Resource Engineering, University of Science and Technology Beijing, Beijing 100083, China
[c] Department of Civil Engineering, Geotechnical Division, Recep Tayyip Erdogan University, Fener, Rize TR53100, Turkey

ARTICLE INFO

ABSTRACT

Fiber reinforced cementitious tailings backfill (FRCTB) is progressively employed in mining industry due to its high strength/stiffness-to-weight ratio. However, the wide use of the FRCTB technique requires further study of the practice of many different types of fibers, either alone or in combination. In this regard, this paper explores the impact of composite (glass-polypropylene) fibers on microstructure of FRCTBs considering weak surface and pore characteristics. The fractures of backfills were quantitatively analyzed by a non-destructive X-ray micro-computed tomography system which permits imagining of the interior microstructures of backfills via the construction of 3D volumetric data in diverse spatial scales. Quantitative parameters cover percent weak surface, porosity, and pore sphericity. The spatial distribution of weak surfaces, pores, and fissures and the bridging effect of fibers were also analyzed based on the 3D reconstruction technique. Adding fibers increased the percentage of FRCTB's weak surface. The greater the glass fiber dose, the larger the percentage of the weak surface. Composite fibers can lessen FRCTB's porosity. The smallest FRCTB porosity was 0.07 % for glass and PP fiber contents of 0.4 wt% and 0.2 wt%, respectively. A rise in glass fiber dose causes a rise in volume of 10—100 mm^3 pore content. Fibers have a greater impact on the volume of 0.1—100 mm^3 pores, and the rise in glass fiber dose deteriorates shape of this type of pores, leading to a reduction in the sphericity of this type of pores. There is a clear correlation between the distribution patterns of weak surfaces, pores, and fissures along the height of the specimens. Weak surfaces and pores are prone to develop as fractures. Fibers can limit the crack expansion in FRCTB. Lastly, this study presents a time- and cost-saving method for analyzing FRCTB's microstructure.

* Corresponding author. State Key Laboratory of High-Efficient Mining and Safety of Metal Mines of Ministry of Education, University of Science and Technology Beijing, Beijing 100083, China.
** Corresponding author. School of Civil and Resource Engineering, University of Science and Technology Beijing, Beijing 100083, China.
*** Corresponding author. State Key Laboratory of High-Efficient Mining and Safety of Metal Mines of Ministry of Education, University of Science and Technology Beijing, Beijing 100083, China.
E-mail addresses: lijiajian0123@163.com (J. Li), sandy_cao@ustb.edu.cn (S. Cao), erol.yilmaz@erdogan.edu.tr (E. Yilmaz).

1.   Introduction

Fiber reinforced cementitious tailings backfill (FRCTB) is a combined material manufactured by fibers [1], tails [2], binders [3], and waters [4]. This emerging new technique has recently received much attention worldwide as a modified underground stope backfill material [5,6]. It has an excellent crack resistance feature compared to cemented tailings backfill (CTB [7—9]). In actual engineering, FRCTB can keep intact under the pressure of surrounding rock and blasting impact [10], effectively solving the problem of ore depletion caused by CTB crushing [11,12]. A large number of researchers have explored the strength features of FRCTB specimens [13—15]. Wang et al. [16] investigated the rubber fiber influence on collapse/strength properties of CTB by means of collapse and uniaxial compression experiments. Xu et al. [17] concluded that as a dose of polypropylene fiber is below 0.3 %, fiber can rise shear strength of CTB-rock interface. Li et al. [18] found that doping with polypropylene fibers can well increase CTB toughness. Currently, most of these studies address the fiber type/content impact on strength/rheological features of FRCTB [19—21]. It is a well-known fact that the strength property of backfilling is very closely linked with its microstructural characteristics [22]. Nevertheless, there are fewer reports on the impact of fibers on FRCTB's microstructure properties [23—25].

Currently, the microstructure of cementitious composites is generally studied for pores [26], fractures [27], and hydration products [28]. The microstructure of fiber-reinforced cementitious matrices is mainly governed through two principal parameters: type [29] and dose [30] of the fibers. It is generally believed that the fibers restrict and hinder crack expansion during FRCTB damage [31,32]. FRCTB has a complex damage pattern [33], changing the cracking type of CTB specimens by the doping of fibers [34]. Li et al. [35] established that damage form of fibreless reinforced composite specimens is mainly tensile damage. FRCTB specimens create a lot of tensile cracks in the primary phase of loading, and later tensile cracks transform into shear cracks, so FRCTB's damage form is mainly shear damage [36—38]. Xue et al. [39] concluded that the doping of fibers enhanced the toughness and crack resistance of CTB. Bending test results show that FRCTB has a cracking but not fracture damage mode [40].

In addition, some scholars point out that the compressive or flexural strength of FRCTB is close to that of CTB, or even slightly reduced [41—43]. On the one hand, the easy agglomeration of fibers has a harmful influence on FRCTB's strength property [44]. On the other hand, Yang et al. [45] suggested that the fibers may have instigated a rise in FRCTB's pore space, which in turn initiated a drop in the strength of fill. As fiber dose becomes higher, the pore number within FRCTB specimens rises significantly and the porosity becomes larger [46]. The deterioration of pore space may affect negatively the whole FRCTB specimens when applied to the actual project [47]. However, no all fibers deteriorate the pore space, which may be closely associated with the dose of fiber [48]. Zhao et al. [49] probed the polyacrylonitrile fiber impact on porosity of FRCTB specimens by the nuclear magnetic resonance technique. Note that doping of polyacrylonitrile fibers could
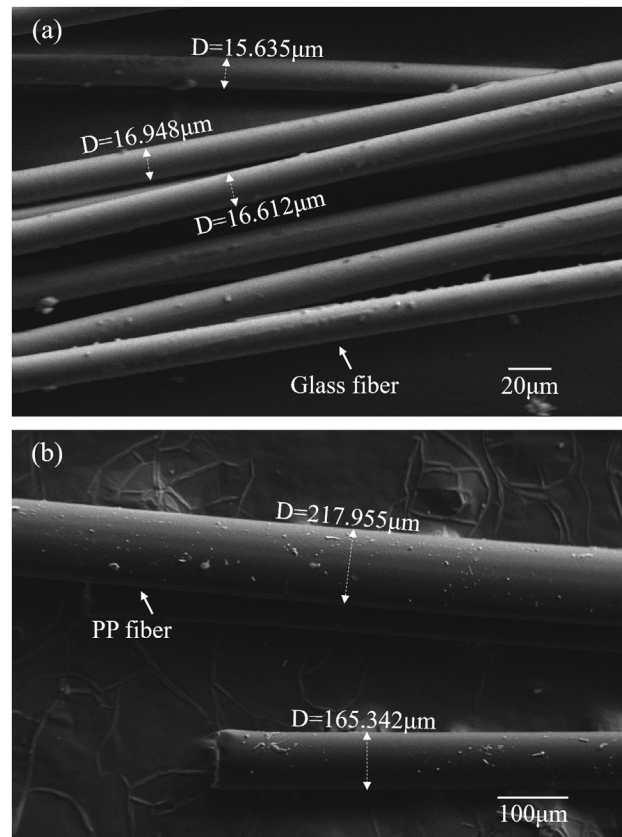
Fig. 1 — The morphological shapes of fibers: (a) glass; and (b) PP.

diminish large pores present within FRCTB specimens, and thus reduce the porosity [50].

In summary, numerous scholars mainly reported the single fiber impact on microstructure of FRCTB specimens. However, no specific researches have been performed on the impact of composite fibers on FRCTB's microstructure. To address this lack of knowledge, this paper deals with the weak surface percentage, porosity, and pore sphericity parameters of composite FRCTBs with glass and polypropylene fibers through uniaxial compressive strength and X-ray microcomputed tomography tests. Accordingly, the originality and significance of the present work are closely linked with the use of 3D reconstruction techniques to inspect the composite fibers' impact on FRCTB's microstructure.

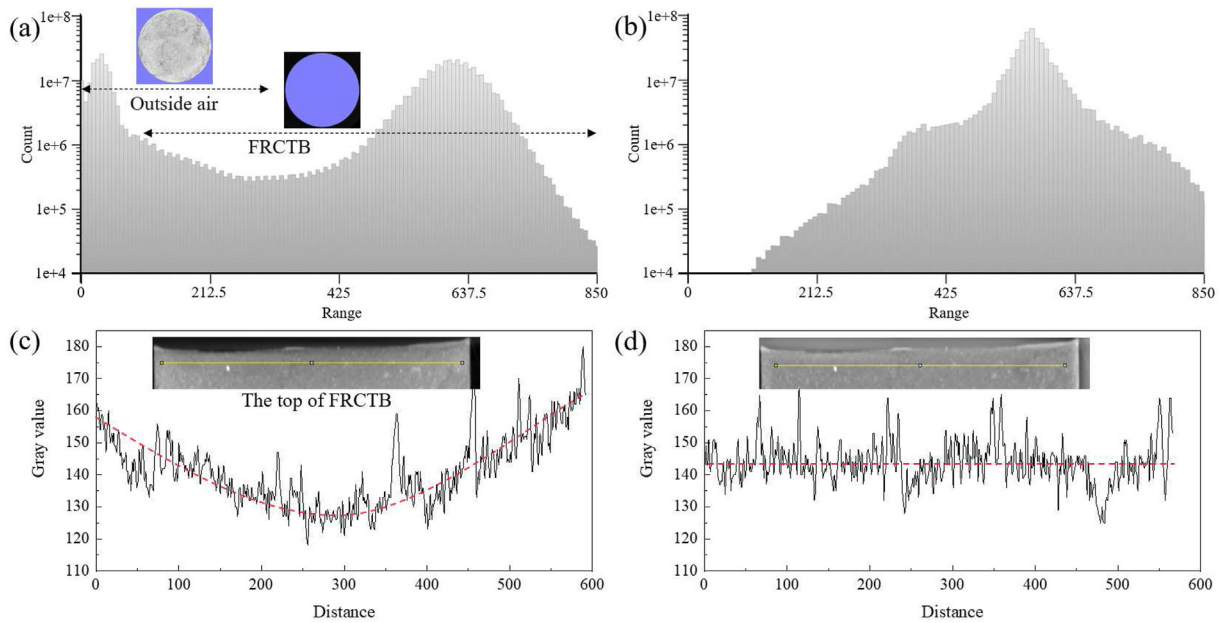## 2.   Materials and methods

2.1.   Materials

FRCTB specimens were manufactured by tungsten tails collected from a mining site in the Yunnan Province, China.

**Table 1 — Physico-mechanical features of glass-PP fibers.**

Fiber name	Size (mm)	Dia. (μm)	Density (g/cm^3)	Tensile strength (MPa)
Glass	12	15—17	2.02	324
PP	12	165—218	0.91	398

Fig. 2 — Histogram of grey scale distribution for the elimination of outside air and end effects for a FRCTB sample.

OPC42.5R was taken as a cementitious agent obtained from Tianjin, China. Tap water present in the laboratory was taken as a blending water. Tungsten tailings' chemistry and grain sizes were measured by an XRF spectrometer and LS-POP laser particle size analyzer. Tailings have a particle size range of 0.1—750 μm. Detailed test results can be found in previous publications [51]. SiO_2 (31.3 wt%) is the main oxide of tungsten tailings. In addition, the elemental iron content in tungsten tails is high (13 wt% Fe_2O_3). Approximately 50 % of tungsten tailings have a particle size greater than 268.659 μm. The surface area average diameter of tungsten tailings D (3,2) is

141.058 μm and the volume average diameter D (4,3) is 297.673 μm. The curvature coefficient (Cc: $D_{30}^2/D_{60} \times D_{10}$) of tungsten tails is 1.27 while their uniformity coefficient (Cu: D_{60}/D_{10}) is 5.58. Tungsten tailings are coarse-grained, having a non-uniform PSD and irregular particle shapes. A recent work [36] has shown that either glass fiber or polypropylene (PP) fiber as a single additive material are effective in improving FRCTB's mechanical and cracking performance. In the present research, a length of 12 mm glass-polypropylene fibers were selected as additive materials. Fig. 1 indicates the morphological shapes of glass-PP fiber. Both fibers have smooth
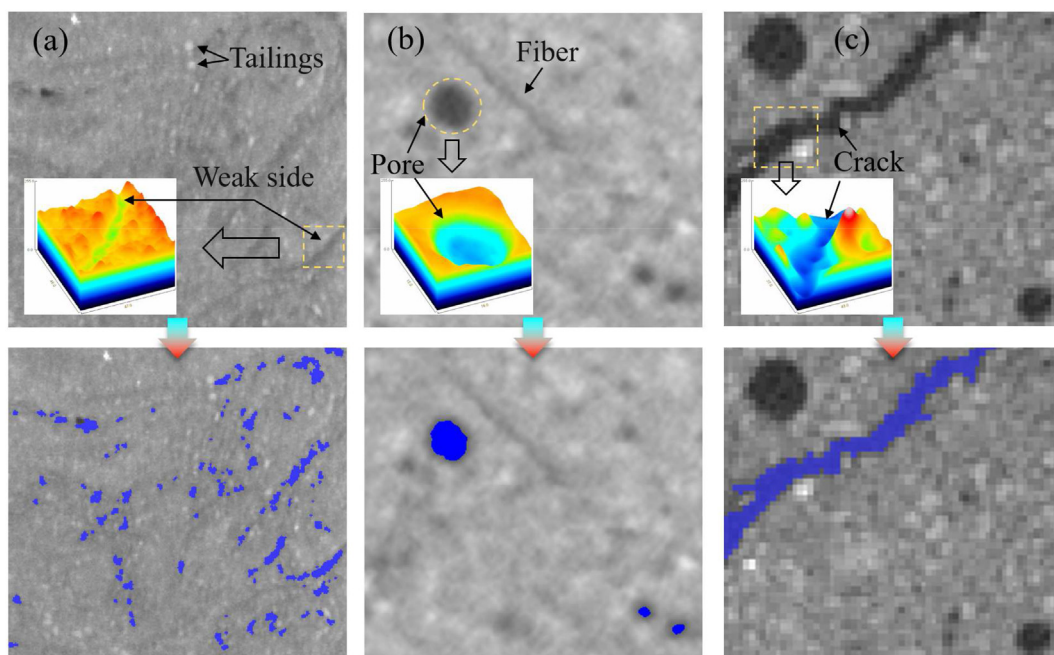
Fig. 3 — Threshold segmentation of different phases in CT scan slice images: (a) weak side; (b) pore; (c) crack.
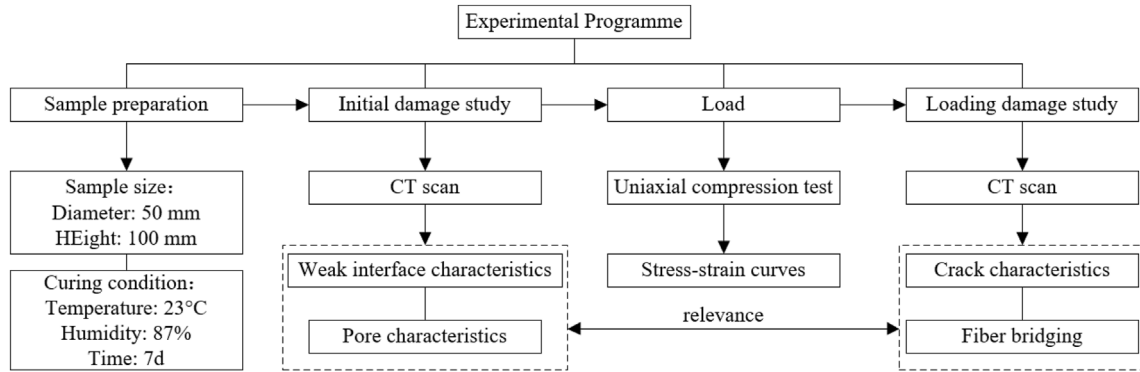
Fig. 4 — A flowchart of the experiments implemented in this study.

surfaces and straight shapes. Table 1 shows the mechanical parameters of two fibers. There is a significant difference between the diameters of two fibers. The diameter of glass fibers is 15—17 μm and the diameter of PP fibers is 165—218 μm. The diameter of polypropylene fiber is 10—13 times the diameter of glass fiber.

2.2. Sample preparation

In this study, FRCTB was prepared using glass and PP fibers. The total quantity of glass-PP fiber is 0.6 wt% (based on total mass of FRCTB solids). The principal reason for using this constant fiber content value is based on an optimization study [51], which provides the best improvement effect with

relatively high mechanical properties having low-cost material. Seven types of FRCTB specimens were designed and manufactured in the laboratory. Specimen IDs are: G0.0-PP0.6, G0.1-PP0.5, G0.2-PP0.4, G0.3-PP0.3, G0.4-PP0.2, G0.5-PP0.1, G0.0-PP0.6. G0.1-PP0.5 represents FRCTB containing a combined fiber dose of 0.6 wt% (0.1 wt% glass fiber + 0.5 wt% PP fiber). G0.0-PP0.0 basically denotes the reinforced cement without fiber (designed as a control group). The content of tungsten tailings and cement is 70 wt% and the content of mixed water is 30 wt%. The mass proportion of cement/ tungsten tailings is 1:6. To disperse fibers evenly, cement, tungsten tails, and fibers were agitated for 180s and some waters were incorporated and continued to be mixed for 180s. Mold used in the experiment was a cylindrical steel mold of
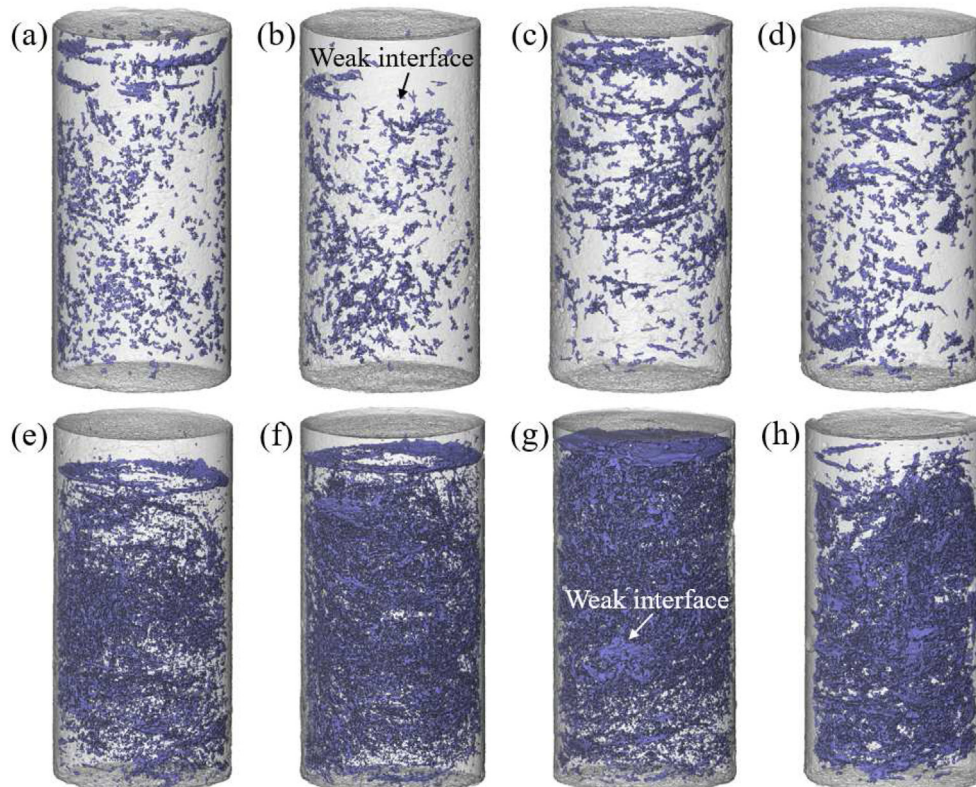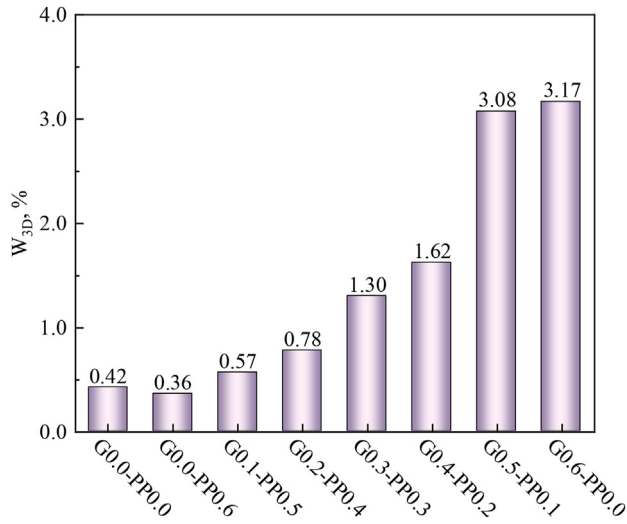

Fig. 5 — 3D reconstruction of the weak surfaces in all samples. (a) G0.0-PP0.0; (b) G0.0-PP0.6; (c) G0.1-PP0.5; (d) G0.2-PP0.4; (e) G0.3-PP0.3; (f) G0.4-PP0.2; (g) G0.5-PP0.1; (h) G0.6-PP0.0.

Fig. 6 — Relationship between W_{3D} and fiber content in all composite fiber-reinforced FRCTB samples.

50×100 mm. Temperature (23 °C and moisture 87 % were chosen as a curing box conditions. Curing age was set to 7 days. A total of 24 samples (3 of each type) were made and the detailed sample preparation procedure can be found in previous work [52].

2.3.   UCS experiment

Consistent with the domestic standard GB/T 17,671-1999, a WDW-200D universal material test press was employed for inspecting FRCTB's strength features. It keeps a mechanical strength test accuracy of ±0.5 %. Press has a displacement (strain) amount of 1 mm per minute throughout loading. UCS/ stress as a function of displacement data of FRCTB are automatically saved by the computer. At the test's end, the backfill specimens were stored in plastic-sealed bags.

2.4.   CT scan experiment

CT scan trial was done on seven FRCTBs and controls before/ after unconfined compression testing. A high-resolution inspection tool entitled (X-ray μ-CT X-ray micro-computed tomography) manufactured by YXLON, Germany was used in the current investigation. Y.XRD 1620 was used as a detector type. A voltage of 220 kV and a current of 2.75Ma were taken as test parameters. The slice image size obtained from the CT scan is 2048×2048, with a pixel size of 34 μm.

2.5.   Slice image processing

2.5.1.   Image preprocessing
During the CT scan, the FRCTB and surrounding air are captured together to form a 2D slice image. This resulted in end effects and unwanted background in the experimental data. External air causes a double peak in the histogram of the grey distribution, as shown in Fig. 2(a). There is a partial overlap of grey values between the external air and FRCTB, which increases the difficulty of threshold segmentation. Fig. 2(c) indicates that end impact refers to uneven distribution of grey values in the same height region at the bottom of the top of FRCTB. At the same level (yellow straight line in
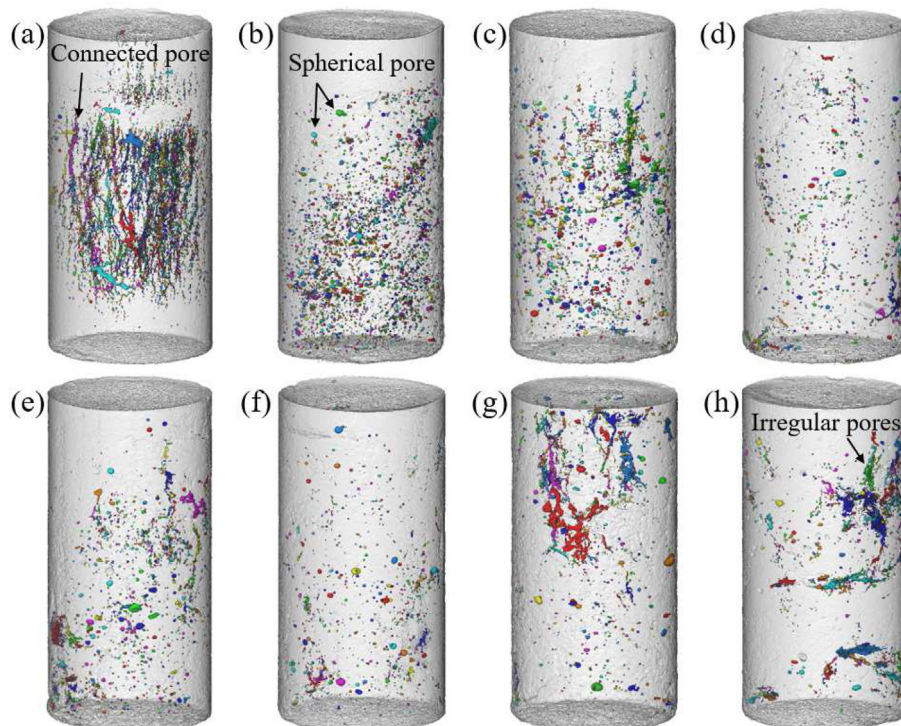
Fig. 7 — 3D reconstruction of pores in all samples. (a) G0.0-PP0.0; (b) G0.0-PP0.6; (c) G0.1-PP0.5; (d) G0.2-PP0.4; (e) G0.3-PP0.3; (f) G0.4-PP0.2; (g) G0.5-PP0.1; (h) G0.6-PP0.0.
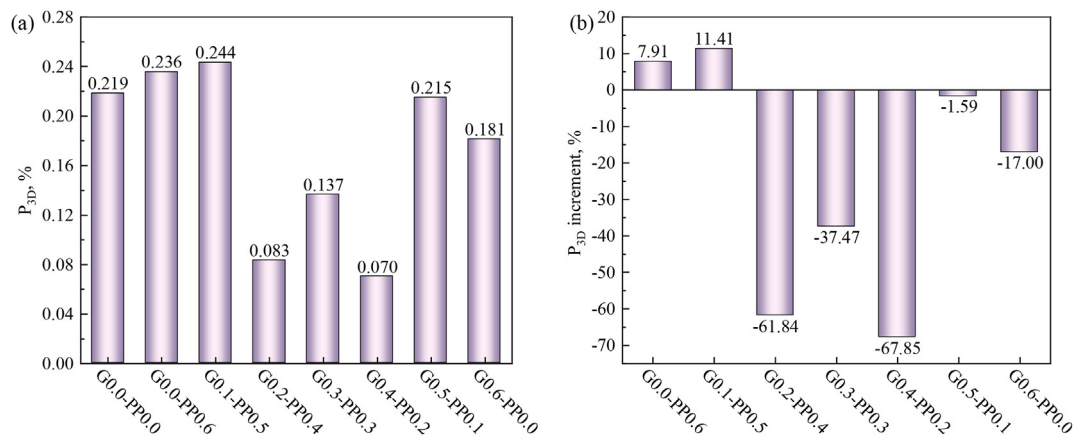
Fig. 8 − Relationship between P_{3D} and fiber content in all composite fiber-reinforced FRCTB samples.

Fig. 2), the grey scale values are lower at the top center axis position of FRCTB and higher on both sides of center axis. The end effects can cause voxels to be mis-selected during image segmentation. Thus, the image is pre-processed before segmentation to eliminate end effects and unwanted background. Fig. 2(b) shows the histogram of grey scale distribution after pre-processing. Fig. 2(d) indicates a grey distribution zone of similar horizontal voxel at the top of FRCTB after pre-treatment, with the end effect largely eliminated.

2.5.2. Segmentation of images

Image segmentation is the process of classifying the voxels of the images acquired during a CT scan test. In this study, voxels were classified by their grey scale values. The size of the greyscale value is linked to local chemical composition [53]. Fig. 3 shows the grey-scale images and threshold segmentation results for three FRCTBs. Six different phases can be found within FRCTB, namely pores, fractures, weak surfaces, FRCTB matrix, tungsten tail particles, and fibers, where pores and fissures have similar grey scale values. When the threshold range is 1−360, most of pores and fissures are covered. Two were further split according to shape differences

to allow separate analyses of the fissures. The weak surface greyscale values lie between pore and FRCTB matrix with a threshold range of 370−550. It should be noted that PP fibers and the weak side are split together. Thus, a secondary process is done on the segmentation results to eliminate PP fibers. 3D reconstructions of segmented weak surfaces, pores, and fractures are carried out and quantified. This part will be discussed in Section 3.

Fig. 4 displays the flow chart covering the three different stages (Stage I: the initial damage work; Stage II: the loading process to specimen; and Stage III: the loading damage work) of the research method followed in the current study.

3.   Results and discussion

3.1.   Weak interface characteristics

Weak surfaces are weak structural surfaces due to localized uneven hydration reactions within CTB. The weak surface is harmful to the mechanical properties of CTB. In FRCTB, fiber agglomerates are more likely to lead to localized inhomogeneous hydration reactions, resulting in the formation of weak
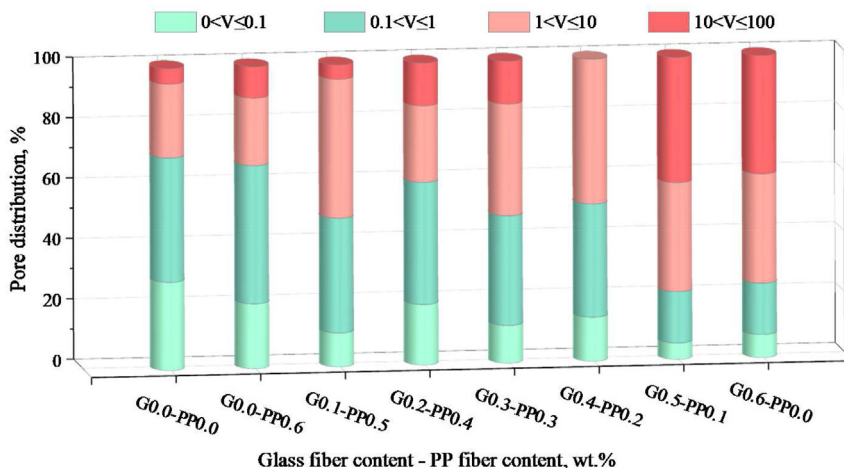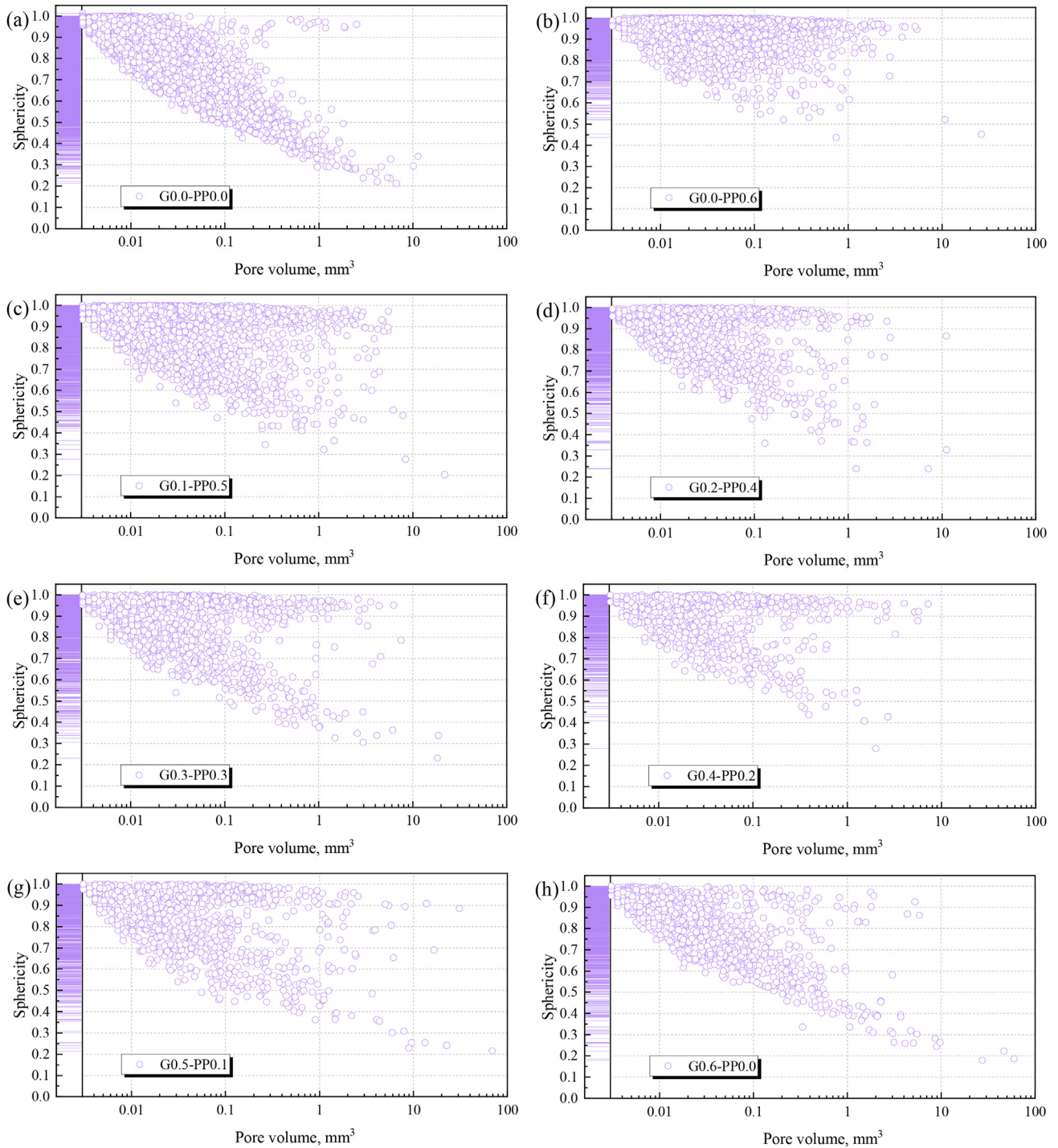

Fig. 9 − Pore volume fraction of all samples obtained by CT scanning.

surfaces in FRCTB. Fig. 5 shows the 3D reconstructed images of the weak surfaces in all samples tested. It can be found that the weak side is chiefly governed by glass fiber dose. As glass fiber dose is below 0.3 wt%, weak surface is randomly dispersed in FRCTB and volume of weak surface is small. When glass fiber dose is greater than or equal to 0.3 wt%, the weak surface within FRCTB increases significantly and the volume of the weak surface is larger.

The weak surface volume was defined as a percentage of FRCTB volume as percentage of weak surface in 3D (W_{3D}). A quantitative analysis of the weak side is shown in Fig. 6. It can be noticed that the weak surface volume fractions of G0.0-PP0.0 and G0.0-PP0.6 are smaller (0.36–0.42 %). Weak surface volume fractions of G0.5-PP0.1 and G0.6-PP0.0 are larger at 3.08 % and 3.17 % respectively. The percentage of weak surfaces increases with increasing glass fiber content.

Fig. 10 – Link between sphericity and pore volume for all samples obtained by CT scanning. (a) G0.0-PP0.0; (b) G0.0-PP0.6; (c) G0.1-PP0.5; (d) G0.2-PP0.4; (e) G0.3-PP0.3; (f) G0.4-PP0.2; (g) G0.5-PP0.1; (h) G0.6-PP0.0.
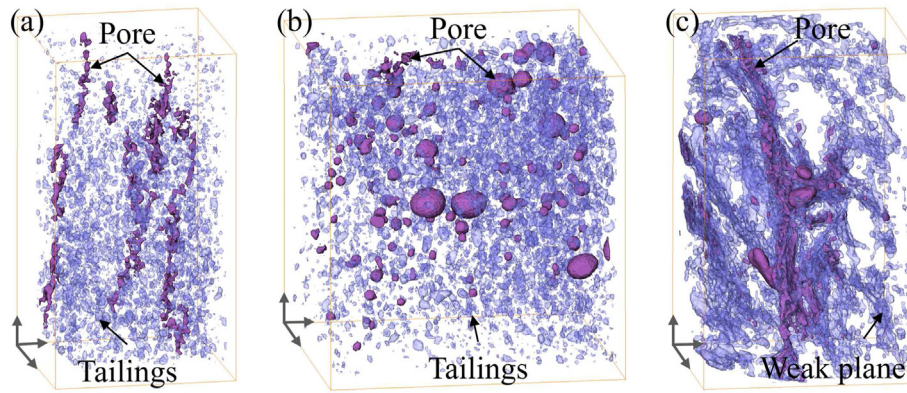
Fig. 11 — 3D reconstructed images of local areas of the sample: (a) G0.0-PP0.0; (b) G0.0-PP0.6; (c) G0.6-PP0.0.

3.2. Pore characteristics

Fig. 7 shows the 3D reconstructed images of the internal pores of all the samples tested. It can be found that fibers possess a noteworthy impact on both spatial distribution and pore shape. The pores in G0.0-PP0.0 are strips of pores distributed axially along the cylindrical sample. The pores are densely distributed in specimen's central zone. Pores within specimen G0.0-PP0.6 are randomly distributed in a disordered manner within the specimen, and the pore shape is predominantly spherical or quasi-spherical. Pores within specimen G0.6-PP0.0 are not uniformly distributed, most of them are irregularly shaped pores and there are fewer spherical pores. The pore structure in FRCTB specimen is complex. Spherical and irregularly shaped pores are randomly distributed within the specimen. The number of pores is low in G0.2-PP0.4 and G0.4-PP0.2. Compared to CTB and single fiber-reinforced CTB specimens, composite fibers optimize the internal pore space of FRCTB.

Quantitative analysis of pore space was based on a three-dimensional reconfiguration model. The pore volume was defined as a percentage of FRCTB volume as 3D Porosity (P_{3D}). Fig. 8 displays the link between P_{3D} and fiber content. The P_{3D} for G0.0-PP0.0 is 0.219 %. The P_{3D} for G0.0-PP0.6, G0.1-PP0.5, G0.5-PP0.1 and G0.6-PP0.0 are closer to that of G0.0-PP0.0 at 0.236 %, 0.244 %, 0.215 % and 0.181 % respectively. P_{3D} growth rates were 7.91 %, 11.41 %, −1.59 %, and −17.00 % respectively. Compared to G0.0-PP0.0, P_{3D} of G0.2-PP0.4, G0.3-PP0.3 and G0.4-PP0.2 was substantially lower, with P_{3D} of 0.083 %, 0.137 % and 0.070 % respectively. P_{3D} was reduced by 61.84 %, 37.47 %, and 67.85 % respectively. The results show that P_{3D} of FRCTB specimen varies little when mixed with a single type of fiber or with a 1:5 or 5:1 mixture of glass-PP fibers. P_{3D} of FRCTB specimen is significantly reduced when glass-PP fibers are mixed in ratios of 2:4, 3:3, and 4:2.

To further inspect the impact of composite fibers on pore distribution in diverse pore volume ranges, pores are categorized as four key types regarding their volume (V): large pores ($10\,mm^3 < V \leq 100\,mm^3$), medium pores ($1\,mm^3 < V \leq 10\,mm^3$), small pores ($0.1\,mm^3 < V \leq 1\,mm^3$), and micro pores ($0\,mm^3 < V \leq 0.1\,mm^3$). Fig. 9 shows percentage of total pore volume for each type of pore spread. As glass fiber dose
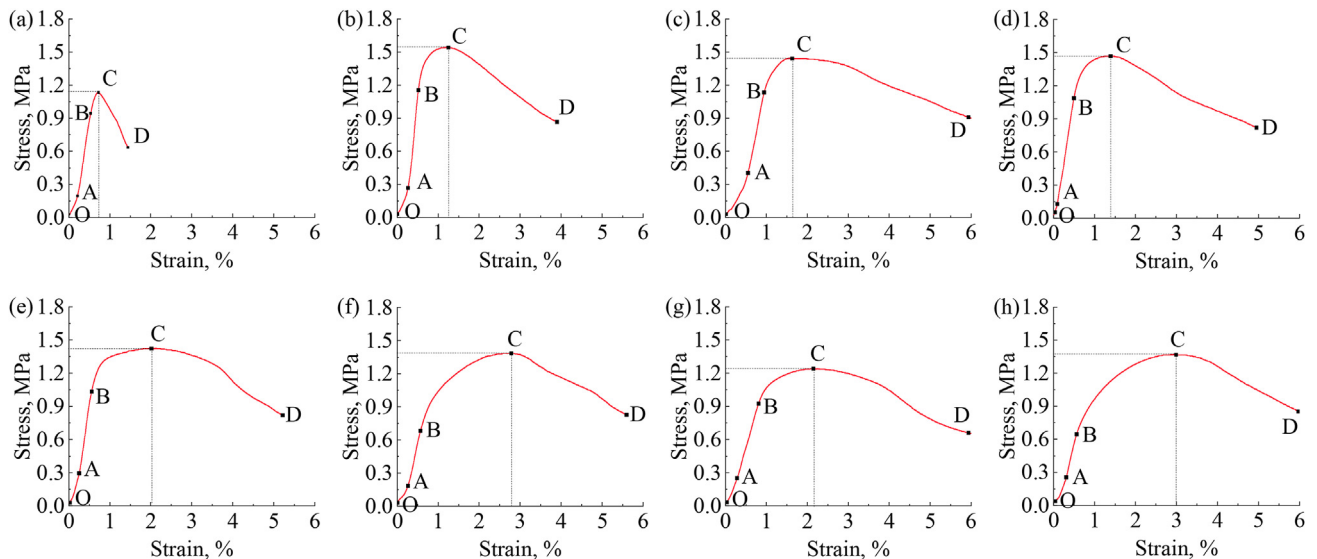

Fig. 12 — Stress-strain curves obtained in uniaxial compression experiments. (a) G0.0-PP0.0; (b) G0.0-PP0.6; (c) G0.1-PP0.5; (d) G0.2-PP0.4; (e) G0.3-PP0.3; (f) G0.4-PP0.2; (g) G0.5-PP0.1; (h) G0.6-PP0.0.

is < 0.5 wt%, FRCTB's main pore type is small-medium pores, which occupy 65.77—85.4 % of total pore volume. Micro pores are the most abundant (11.24—21.5 %) and large pores are the least abundant (0—14.24 %). When the glass fiber content is ≥ 0.5 wt%, FRCTB's main pore type is large pores, which inhabit 39.2—41.47 % of total pore volume. Medium-small pores are the next most abundant (53.08—53.16 %) and micro pores are the least abundant (5.46—7.64 %). This indicates that large pores' amount rises purposely at higher glass fiber contents (≥0.5 wt%).

To quantify the effect of composite fibers on pore shape, scatter plots of pore sphericity versus volume were plotted for different FRCTB pores (Fig. 10). The nearer the pore sphericity value is 1, the closer the shape of pores is a sphere. The sphericity of the micropores of all samples was less than 0.5. This indicates that the composite fibers do not affect the shape of micropores. The small-medium pores' sphericity of G0.0 - PP0.0 is mainly 0.2—1. The small-medium pores' sphericity of G0.0-PP0.6 is mainly 0.5—1. When glass fiber content rises, the small-medium pores' sphericity decreases. The G0.0-PP0.6 large pores sphericity is approximately 0.5, while the G0.6-PP0.0 large pores sphericity is approximately 0.2. In general, PP fibers optimize the shape of small, medium, and large pores. However, a rise in glass fiber dose can cause deterioration in shape of such pores.

3.3.   Effect of fiber on initial damage

Initial damage such as pores, micro-cracks, and weak surfaces will certainly form during the making of the cement polymer. According to the analysis in sections 3.1 and 3.2, the initial damage within the sample is influenced by the composite fibers. In this study, G0.0-PP0.0 was prepared from coarse tailings and cement. Coarse tailings have poor water retention properties. During sample curing, moisture is lost along the axial direction of the cylindrical sample through the interstices of the tailings particles by a gap at the bottom of mold. Fig. 11(a) indicates that allied pore numbers are formed in G0.0-PP0.0 distributed along the axial direction. Adding fibers may alter the original arrangement of the solid particles and trap large amounts of free water [51,52]. Hence, it is difficult to observe the formation of connected pores in FRCTB due to water loss. In addition, the pore space also changes from an axial distribution to a random distribution (Fig. 11(b)). Compared to PP fibers, glass fibers have a higher aspect ratio. This can lead to the agglomeration of glass fibers within FRCTB [54]. The glass fiber agglomerates lead to a non-uniform hydration reaction within FRCTB and a reduction in FRCTB compactness. Glass fiber agglomerates may be the main reason for the formation of irregular large pores and weak surfaces within FRCTB, as shown in Fig. 11(c).

PP fiber monofilaments are larger in diameter, while glass fibers are finer and more numerous. In the composite fiber system, glass fiber fills void present in PP fibers and PP fibers avoid agglomeration with glass fibers. The synergistic impact of composite fibers causes a drop in 3D porosities in FRCTB. According to analysis in section 3.2, the doping of single or composite fibers has little effect on the micro pores within FRCTB. Several studies have publicized that micropores are related to cementitious agent content and hydration properties [43,44]. Nevertheless, fiber incorporation does not distress the hydration characteristics of the binder. Consequently, no effect of fibers on micropores was found during the pore sphericity analysis.
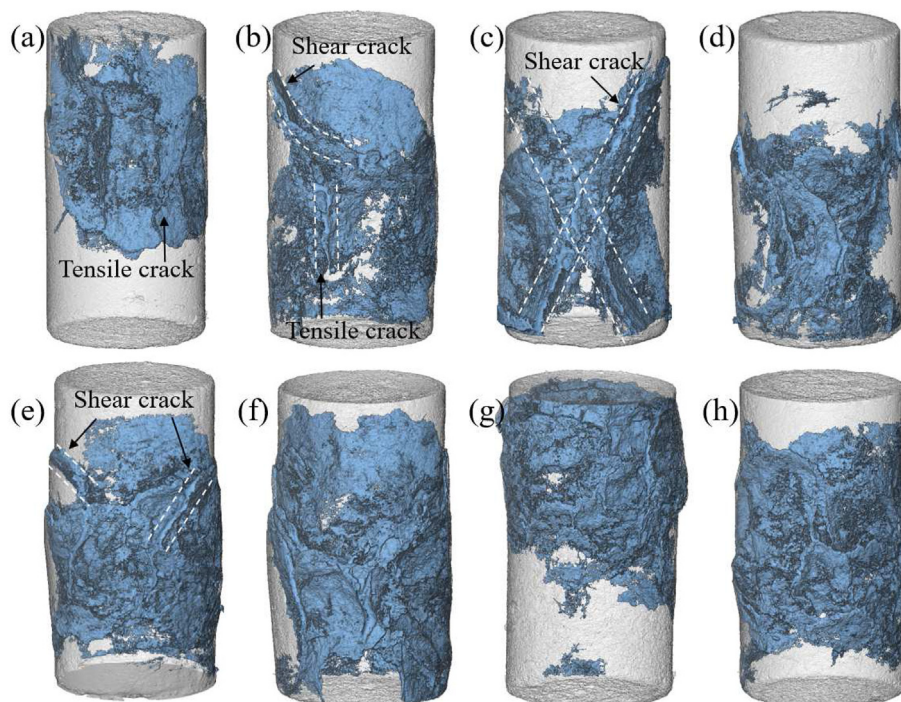

Fig. 13 — 3D reconstruction of the main crack in all samples. (a) G0.0-PP0.0; (b) G0.0-PP0.6; (c) G0.1-PP0.5; (d) G0.2-PP0.4; (e) G0.3-PP0.3; (f) G0.4-PP0.2; (g) G0.5-PP0.1; (h) G0.6-PP0.0.

3.4. Stress-strain curves

The progress of damage in the FRCTB could be explained by inspecting the stress-strain trends taken from specimens. Fig. 12 demonstrates these trends for all backfill specimens obtained during the uniaxial compression experiments. Basically, specimens' stress-strain trends could be assessed in 4 different steps: (i) compaction (OA); (ii) linear elastic (AB); (iii) strain softening (BC); and (iv) crack propagation (CD). The strain value at point B of specimens' stress-strain curve is less than 1 %. The curve's BC section changes significantly with rising glass fiber content, that is, the peak strain of FRCTB

increases. This may be related to the fact that an augmentation in glass fiber dosage gives rise to a growth in the weak surface within FRCTB. This results in a large strain of FRCTB in the strain softening stage.

3.5. Effect of initial damage on crack

Fig. 13 indicates a three-dimensional reconstructed view of main crack in all samples. FRCTB has a high capacity for radial deformation. For example, G0.0-PP0.0 in Fig. 13(a) has no significant radial deformation. However, FRCTB has significant radial deformation, especially the G0.3-PP0.3 and
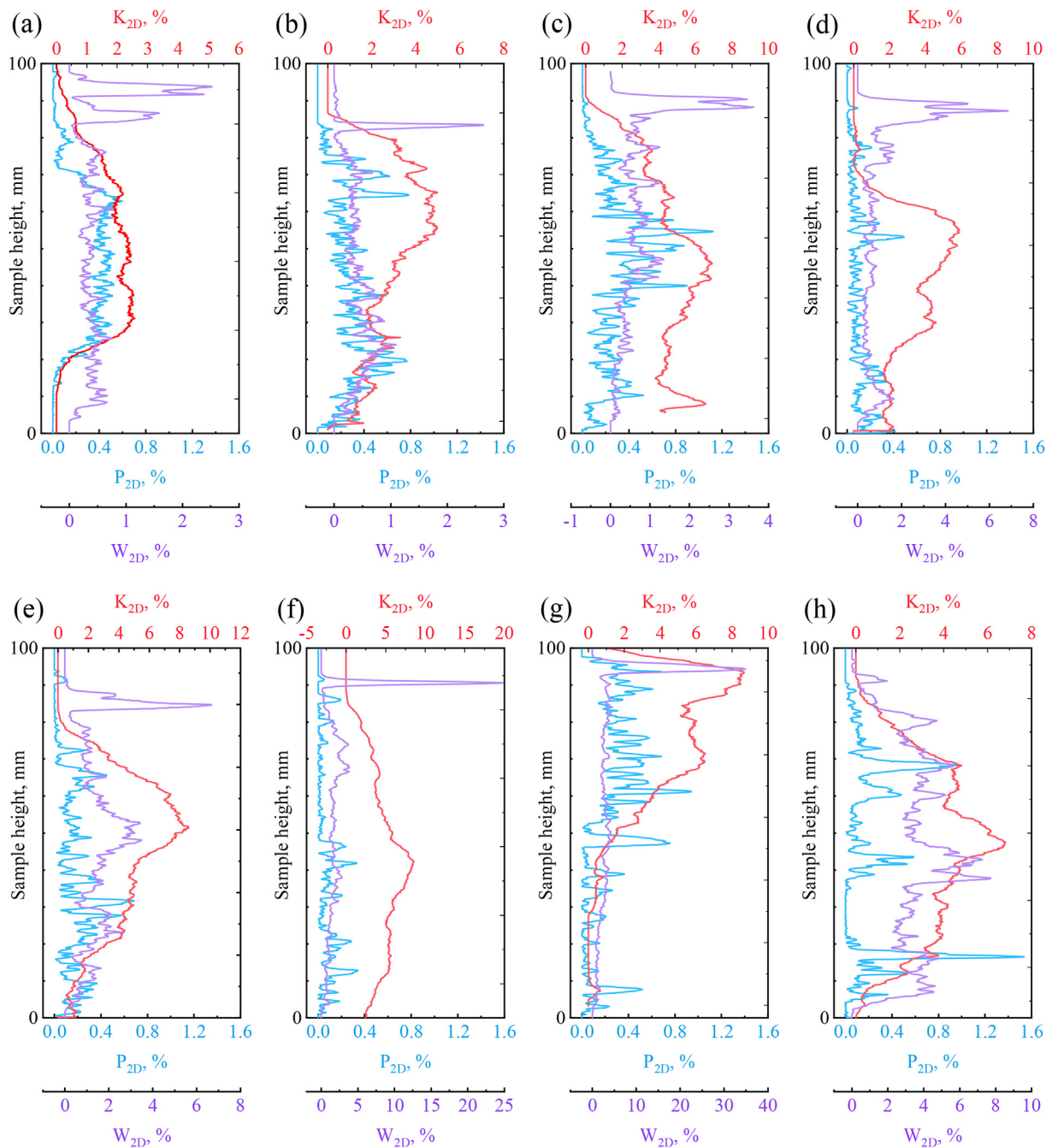

Fig. 14 − Weak interface, pores, and cracks along sample height distribution curve. (a) G0.0-PP0.0; (b) G0.0-PP0.6; (c) G0.1-PP0.5; (d) G0.2-PP0.4; (e) G0.3-PP0.3; (f) G0.4-PP0.2; (g) G0.5-PP0.1; (h) G0.6-PP0.0.

G0.4-PP0.2 radial deformations, as shown in Fig. 13(e) and (f). Cracking in G0.0-PP0.0 is mainly tensile cracking, and its damage mode is mainly expressed as tensile damage. The cracking in FRCTB is mainly shear cracking, with a small amount of tensile cracking present, and the damage mode exhibits shear-tensile damage. For example, Fig. 13(c) indicates a clear "X" shaped shear crack while Fig. 13(b) indicates partial tensile damage. In combination by Fig. 7, one can infer that fracture distribution correlates with the pore distribution. For example, pores in G0.0-PP0.0 and G0.5-PP0.1 are not evenly distributed, with most of the pores being located in the middle and top of sample. From Fig. 13(a) and (g) it can be noticed that G0.0-PP0.0 and G0.5-PP0.1 fissures are also present in the middle/top of sample. Several studies have shown that samples are susceptible to stress concentrations in the pore region when subjected to external loads and fractures are created.

The fracture zone in the slice image was defined as a fraction of sample cross-sectional zone when 2D damage factor (K_{2D}). The pore zone in the slice image was defined as a fraction of cross-sectional zone of the sample as a porosity in 2D (P_{2D}). The area of the weak side in the slice image was defined as a percentage of the sample cross-sectional area as W_{2D}. A quantitative analysis of the initial damage (pores and weak surfaces) about fractures is shown in Fig. 14. The large point in W_{2D} curve at specimen's top is because experimenter performed secondary grouting of the sample with high water loss. Secondary grouting does not affect the experimental conclusions, as the three curves are barely correlated at the secondary grouting location.

K_{2D} and P_{2D} curves of G0.0-PP0.0 have a consistent trend and are largely uncorrelated with W_{2D}, this suggests that fractures in CTB are mainly influenced by the pore distribution and are not related to the weak surface. The greater the 2D porosity within FRCTB specimen, the larger the fracture zone of fill specimen after damage. The three curves of FRCTB do not follow the same trend, due to the influence of the fibers. However, correlations between the curves can be found in some of the samples or parts of a particular sample. For example, the three curves of G0.1-PP0.5 and G0.6-PP0.0 have essentially the same trend. This suggests that the fracture distribution in FRCTB is influenced by a combination of pore and weak surface distribution. The trends of K_{2D} and W_{2D} curves in G0.3-PP0.3 are extremely similar in the middle of sample. This suggests that the impact of weak surfaces on fractures is greater than the influence of pore space on fractures in this area. In general, fractures within CTB are influenced by pore space and fractures in FRCTB are influenced by a combination of pore space and weak surfaces.

3.6. Effect of fiber on crack propagation

FRCTB has a high resistance to cracking. This depends on the restriction of fracture extension by the fibers, namely fibers' bridging impact [55]. In flexural test, FRCTB specimen had a single fissure and a large fissure opening. The bridging impact of fibers present within FRCTB specimen is therefore more easily observed [56–58]. However, fibers' bridging impact on cracks within sample is difficult to observe directly in uniaxial compression experiments. Researchers have observed localized areas of FRCTB by SEM observations, revealing fiber' bridging and cementing effect at microscopic scale [59,60]. However, the majority of results are on the bridging of microcracks by monofilament fibers. Fibers are not evenly distributed in FRCTB. A study shows that glass fibers are distributed in clusters in FRCTB [61].

Fig. 15 shows the clustered distribution of glass fibers within FRCTB. The clustered glass fibers do not exhibit a significant bridging effect, but rather hinder the creation of fissures in areas near the fibers. As can be seen in Fig. 15, a crack with a width of 1 mm was formed within FRCTB under external loading. The fissure runs diagonally through the tufted fibers at an angle of 23.67° fibers. The clustered fibers hinder the creation of fissures and only partial microcracks are formed near the fibers. PP fibers are large in diameter and monofilament PP fibers can be directly detected in CT scan results.

Fig. 16 indicates the bridging effect of PP fibers on macroscopic cracks. Since PP fibers have a smaller aspect ratio, they are more uniformly dispersed within FRCTB than glass fibers. PP fibers rely on the bond with FRCTB matrix to limit the expansion of macroscopic fractures. Thus, FRCTB has a high capacity for radial deformation.
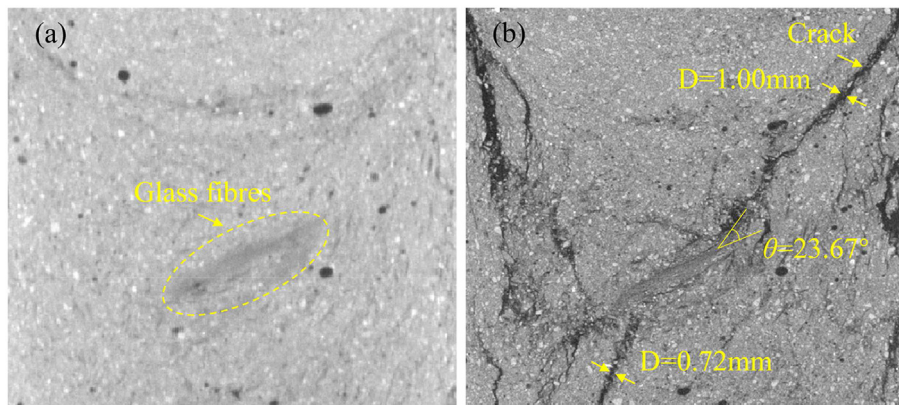

Fig. 15 – Slice images of G0.1-PP0.5 before (a) and after (b) uniaxial compression.
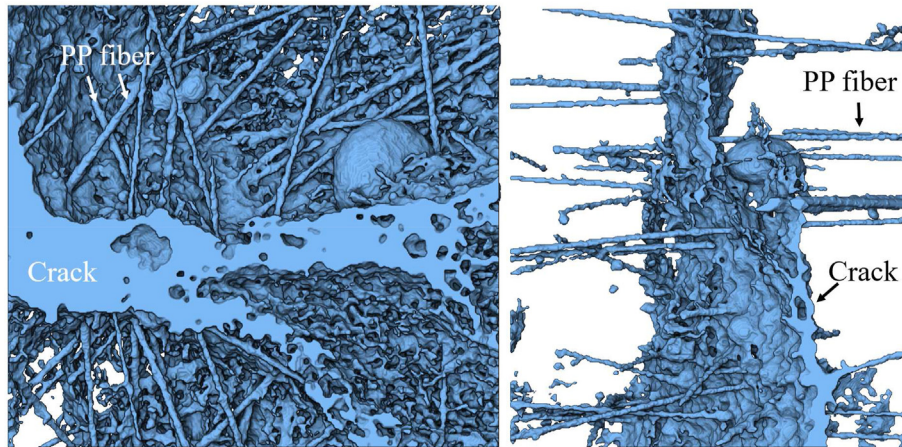
Fig. 16 — 3D reconstruction results for cracks bridged by fibers.

4. Conclusions

The effect of composite fibers on weak surfaces, pores and fractures in FRCTB was analyzed by CT scan test. The spatial distribution of weak surfaces, pores, and fractures has been visualized and analyzed based on 3D reconstruction techniques. Weak surfaces and pores were quantified by parameters such as percentage of weak surface, porosity, and sphericity. The influence of weak surfaces and pores on cracking is analyzed based on the spatial distribution pattern of weak surfaces, pores, and cracks in FRCTB. The main conclusions are as follows.

o Adding fibers leads to a rise in the volume of weak surface in FRCTB. The percentage of weak surfaces in FRCTB surges with rising glass fiber dose. The G0.0-PP0.6 weak surface percentage is the smallest at 0.36 % and G0.6-PP0.0 weak surface percentage is the largest at 3.17 %.
o The addition of fibers alters the spatial distribution pattern of pores. The pores in CTB specimen are connected pores distributed axially along the cylindrical sample, mainly concentrated in the middle of the sample.
o As PP fiber dose is beyond 0.1 wt%, pores in FRCTB are mostly spherical or quasi-spherical and the pores are randomly distributed within the sample. As glass fiber dose is above 0.4 wt%, pores in FRCTB are mostly irregular large pores.
o Composite fibers can reduce 3D porosity of FRCTB. 3D porosity of G0.0-PP0.6 and G0.6-PP0.0 is 0.236 % and 0.181 % respectively. 3D porosity of G0.4-PP0.2 is 0.070 %. The composite fiber reduces the 3D porosity by 61.33—70.34 %.
o The increased glass fiber dose causes a major increase in percentage of large pores to pores' total volume. The percentage of large pore volume increases from 0-14.24 % to 39.20—41.47 % when the glass fiber content is greater than or equal to 0.5 wt%.
o Fibers influence the shape of the pores, except for micropores. An increase in PP fiber content optimizes the pore shape and leads to a rise in pore sphericity. However, a rise in glass fiber dose deteriorates pore shape and leads to a drop in pore sphericity.

o The fracture distribution within CTB is well correlated with the pore distribution and not with weak surface. FRCTB cracking is affected by a combination of weak surfaces and porosity. The clustered fibers also hinder crack extension. PP fiber has a major linking effect on cracks.

Although the findings obtained within the scope of this study will provide researchers with important information and new perspectives, there are still some key issues that need to be executed experimentally and numerically. In this context, the authors are currently carrying out important studies to understand the subject in detail and to add the missing issues to the present literature. In upcoming studies, researchers will concentrate the numerical model of cemented backfills with PP and glass fibers, exploring composite fibers' reinforcement mechanism. The shape of fiber distributions, energy and crack distribution patterns in FRCTB samples with different height/diameter ratios, especially those exposed to dynamic effects, will be another aspect of the examination. Besides, the surface treatment of the fibers, which is a shortcoming of the current study, constitutes the main focus of the authors' future researches.

Declaration of competing interest

The authors declare that they have no known competing financial interests or personal relationships that could have appeared to influence the work reported in this paper.

Acknowledgments

REFERENCES

[1] Zhao Z, Cao S, Yilmaz E. Polypropylene fiber effect on flexural strength, toughness, deflection, failure mode and

microanalysis of cementitious backfills under three-point bending conditions. Minerals 2023;13(9):1135.

[2] Adrianto LR, Pfister S. Prospective environmental assessment of reprocessing and valorization alternatives for sulfidic copper tailings. Resour Conserv Recycl 2022;186:106567.

[3] Arunachalam KP, Avudaiappan S, Maureira N, Filho FDCG, Monteiro SN, Batista ID, et al. Innovative use of copper mine tailing as an additive in cement mortar. J Mater Res Technol 2023;25:2261–74.

[4] Nasharuddin R, Luo G, Robinson N, Fourie A, Johns ML, Fridjonsson EO. Cemented paste backfill compressive strength enhancement via systematic water chemistry optimization. Construct Build Mater 2022;347:128499.

[5] Wang A, Cao S, Yilmaz E. Quantitative analysis of pore characteristics of nanocellulose reinforced cementitious tailings fills using 3D reconstruction of CT images. J Mater Res Technol 2023;26:1428–44.

[6] Xue GL, Yilmaz E, Wang Y. Progress and prospects of mining with backfill in metal mines in China. Int J Miner Metall Mater 2023;30(8):1455–73.

[7] Gao RG, Zhou KP, Zhou YL, Yang C. Research on the fluid characteristics of cemented backfill pipeline transportation of mineral processing tailings. Alex Eng J 2020;59(6):4409–26.

[8] Benzaazoua M, Belem T, Yilmaz E. Novel lab tool for paste backfill. Can Min J 2006;127(3):31–2.

[9] Liu L, Xin J, Huan C, Zhao YJ, Fan X, Guo LJ, et al. Effect of curing time on the mesoscopic parameters of cemented paste backfill simulated using the particle flow code technique. Int J Miner Metall Mater 2020;28(4):590–602.

[10] Yin SH, Hou YQ, Chen X, Zhang MZ, Du HH, Gao C. Mechanical behavior, failure pattern and damage evolution of fiber-reinforced cemented sulfur tailings backfill under uniaxial loading. Construct Build Mater 2022;332:127248.

[11] Yan B, Jia H, Yang Z, Yilmaz E, Liu H. Goaf instability in an open pit iron mine triggered by dynamics disturbance: a large-scale similar simulation. Int J Min Reclamat Environ 2023;37(8):606–29.

[12] Xu WB, Li QL, Zhang YL. Influence of temperature on compressive strength, microstructure properties and failure pattern of fiber-reinforced cemented tailings backfill. Construct Build Mater 2019;222:776–85.

[13] Chen X, Shi XZ, Zhou J, Chen QS, Li EM, Du XH. Compressive behavior and microstructural properties of tailings polypropylene fibre-reinforced cemented paste backfill. Construct Build Mater 2018;190:211–21.

[14] Yilmaz E, Belem T, Benzaazoua M, Kesimal A, Ercikdi B, Cihangir F. Use of high-density paste backfill for safe disposal of copper/zinc mine tailings. Gospodarka Surowcami Mineralnymi-Mineral Resources Management 2011;27(3):81–94.

[15] He W, Liu L, Fang ZY, Gao YH, Sun WJ. Effect of polypropylene fiber on properties of modified magnesium-coal-based solid waste backfill materials. Construct Build Mater 2023;362:129695.

[16] Wang YY, Yu ZQ, Wang HW. Experimental investigation on some performance of rubber fiber modified cemented paste backfill. Construct Build Mater 2021;271:121586.

[17] Xu XQ, An N, Fang K. Experimental investigation into the temperature effect on the shear behavior of the fiber-reinforced interface between rock and cemented paste backfill. Construct Build Mater 2022;356:129280.

[18] Li JJ, Cao S, Yilmaz E. Characterization of macro mechanical properties and microstructures of cement-based composites prepared from fly ash, gypsum and steel slag. Minerals 2022;12(1):6.

[19] Yan ZP, Yin SH, Chen X, Wang LM. Rheological properties and wall-slip behavior of cemented tailing-waste rock backfill (CTWB) paste. Construct Build Mater 2022;324:126723.

[20] Koohestani B, Mokhtari P, Yilmaz E, Mahdipour F, Darban AK. Geopolymerization mechanism of binder-free mine tailings by sodium silicate. Construct Build Mater 2021;268:121217.

[21] Hou YQ, Yin SH, Chen X, Zhang MZ, Yang SX. Study on characteristic stress and energy damage evolution mechanism of cemented tailings backfill under uniaxial compression. Construct Build Mater 2021;301:124333.

[22] Kasap T, Yilmaz E, Sari M, Karasu S. Predicting long-term impact of cementitious mine fill considering sand as a copper-tailings substitution. Powder Technol 2023;428:118887.

[23] Loan I, Libos S, Cui L, Liu XR. Effect of curing temperature on time-dependent shear behavior and properties of polypropylene fiber-reinforced cemented paste backfill. Construct Build Mater 2021;311:125302.

[24] Wang AA, Cao S, Yilmaz E. Influence of types and contents of nano cellulose materials as reinforcement on stability performance of cementitious tailings backfill. Construct Build Mater 2022;344:128179.

[25] Yu Z, Shi XZ, Chen X, Zhou J, Qi CC, Chen QS, et al. Artificial intelligence model for studying unconfined compressive performance of fiber-reinforced cemented paste backfill. Trans Nonferrous Metals Soc China 2021;31:1087–102.

[26] Li JJ, Cao S, Song WD. Distribution development of pore/crack expansion and particle structure of cemented solid-waste composites based on CT and 3D reconstruction techniques. Construct Build Mater 2023;376:130966.

[27] Yang J, Zhao K, Yu X, Yan YJ, He ZW, Zhou Y, et al. Fracture evolution of fiber-reinforced backfill based on acoustic emission fractal dimension and b-value. Cement Concr Compos 2022;134:104739.

[28] Chakilam S, Cui L. Effect of polypropylene fiber content and fiber length on the saturated hydraulic conductivity of hydrating cemented paste backfill. Construct Build Mater 2020;262:120854.

[29] Huang ZQ, Cao S, Yilmaz E. Investigation on the flexural strength, failure pattern and microstructural characteristics of combined fibers reinforced cemented tailings backfill. Construct Build Mater 2021;300:124005.

[30] Cao S, Xue GL, Yilmaz E, Yin Z. Assessment of rheological and sedimentation characteristics of fresh cemented tailings backfill slurry. Int J Min Reclamat Environ 2021;35(5):319–35.

[31] Wang AA, Cao S, Yilmaz E. Effect of height to diameter ratio on dynamic characteristics of cemented tailings backfills with fiber reinforcement through impact loading. Construct Build Mater 2022;322:126448.

[32] Yang J, Zhao K, Yu X, Yan YJ, He ZW, Lai YM, et al. Crack classification of fiber-reinforced backfill based on Gaussian mixed moving average filtering method. Cement Concr Compos 2022;134:104740.

[33] Qin SW, Cao S, Yilmaz E, Li JJ. Influence of types and shapes of 3D printed polymeric lattice on ductility performance of cementitious backfill composites. Construct Build Mater 2021;307:124973.

[34] Zhang LJ, Mo HK, Yap SP, Gencel O, Ling TC. Effect of fibers addition on mechanical properties of eco-friendly phosphogypsum-based composite at high temperatures. J Build Eng 2022;61:105247.

[35] Li Y, Su YQ, Tan TK, Zheng XT, Sheng JL. Pore structure and splitting tensile strength of hybrid Basalt Polypropylene fiber reinforced concrete subjected to carbonation. Construct Build Mater 2021;297:123779.

[36] Xue GL, Yilmaz E, Song WD, Yilmaz E. Influence of fiber reinforcement on mechanical behavior and microstructural properties of cemented tailings backfill. Construct Build Mater 2019;213:275–85.

[37] Yi XW, Ma GW, Fourie A. Centrifuge model studies on the stability of fibre-reinforced cemented paste backfill stopes. Geotext Geomembranes 2018;46:396–401.

[38] Zhang H, Cao S, Yilmaz E. Influence of 3D-printed polymer structures on dynamic splitting and crack propagation behavior of cementitious tailings backfill. Construct Build Mater 2022;343:128137.

[39] Xue GL, Yilmaz E, Song WD, Cao S. Mechanical, flexural and microstructural properties of cement-tailings matrix composites: effects of fiber type and dosage. Composites Part B 2019;172:131–42.

[40] Xue GL, Yilmaz E, Feng GR, Cao S. Bending behavior and failure mode of cemented tailings backfill composites incorporating different fibers for sustainable construction. Construct Build Mater 2021;289:123163.

[41] Wang S, Song XP, Chen QS, Wang XJ, Wei ML, Ke YX, et al. Mechanical properties of cemented tailings backfill containing alkalized rice straw of various lengths. J Environ Manag 2020;276:111124.

[42] Zhang H, Cao S, Yilmaz E. Carbon nanotube reinforced cementitious tailings composites: links to mechanical and microstructural characteristics. Construct Build Mater 2023;365:130123.

[43] Wang Y, Zhang SH, Niu DT, Fu Q. Quantitative evaluation of the characteristics of air voids and their relationship with the permeability and salt freeze-thaw resistance of hybrid steel polypropylene fiber–reinforced concrete composites. Cement Concr Compos 2022;125:104292.

[44] Qin S, Cao S, Yilmaz E. Employing U-shaped 3D printed polymer to improve flexural properties of cementitious tailings backfills. Construct Build Mater 2022;320:126296.

[45] Yang RJ, Zeng Q, Peng Y, Wang HL, Wang ZD. Anomalous matrix and interlayer pore structure of 3D-printed fiber-reinforced cementitious composites. Cement Concr Res 2022;157:106829.

[46] Huang ZQ, Cao S, Yilmaz E. Microstructure and mechanical behavior of cemented gold/tungsten mine tailings-crushed rock backfill: effects of rock gradation and content. J Environ Manag 2023;339:117897.

[47] Chen SC, Gao MY, Lin WT, Liang JF, Li DW. Effects of incorporating large quantities of copper tailings with various particle sizes on the strength and pore structure of cement-based materials. Construct Build Mater 2022;329:127150.

[48] McLean J, Cui L. Multiscale geomechanical behavior of fiber-reinforced cementitious composites under cyclic loading conditions – a review. Frontiers in Materials 2021;8:759126.

[49] Zhao K, He ZW, Yang J, Yan YJ, Yu X, Zhou Y, et al. Investigation of failure mechanism of cement-fiber-tailings matrix composites using digital image correlation and acoustic emission. Construct Build Mater 2022;335:127513.

[50] Zhang YT, Fan ZW, Zhu XY. Effect of multi-minerals on the mechanical behavior and pore structure of fiber reinforced internal-cured green concrete. J Clean Prod 2022;359:132075.

[51] Li JJ, Cao S, Yilmaz E, Liu YP. Compressive fatigue behavior and failure evolution of additive fiber-reinforced cemented tailings composites. Int J Miner Metall Mater 2022;29:345–55.

[52] Li D, Niu DT, Fu Q, Luo DM. Fractal characteristics of pore structure of hybrid Basalt–Polypropylene fibre-reinforced concrete. Cement Concr Compos 2020;109:103555.

[53] Brisard S, Serdar M, Monteiro PJM. Multiscale X-ray tomography of cementitious materials: a review. Cement Concr Res 2020;128:105824.

[54] Guler S, Akbulut ZF. Effect of high-temperature on the behavior of single and hybrid glass and basalt fiber added geopolymer cement mortars. J Build Eng 2022;57:104809.

[55] Zhang XD, Pang S, Su L, Geng J, Cai G, Liu J. Triaxial mechanical properties and microscopic characterization of fiber-reinforced cement stabilized aeolian sand-coal gangue blends. Construct Build Mater 2022;346:128481.

[56] Zhang H, Cao S, Yilmaz E. Polymer shape effect on damage evolution, internal defects and crack propagation of 3D-printed polymer-based cementitious backfill. Construct Build Mater 2023;406:133386.

[57] Yang YY, Zhou Q, Deng Y, Lin JH. Reinforcement effects of multi-scale hybrid fiber on flexural and fracture behaviors of ultra-low-weight foamed cement-based composites. Cement Concr Compos 2022;128:104422.

[58] Zhou N, Du EB, Zhang JX, Zhu CL, Zhou HQ. Mechanical properties improvement of Sand-Based cemented backfill body by adding glass fibers of different lengths and ratios. Construct Build Mater 2021;280:122408.

[59] Alp I, Deveci H, Sungun YH, Yilmaz AO, Kesimal A, Yilmaz E. Pozzolanic characteristics of a natural raw material for use in blended cements. Iran J Sci Technol Trans B-Eng 2009;33:291–300.

[60] Yin SH, Zhou Y, Wang L, Pan J, Kou YY. Setting, bleeding, and hardening strength properties of coarse aggregate backfill slurry. Case Stud Constr Mater 2022;17:e01667.

[61] Huang ZQ, Yilmaz E, Cao S. Analysis of strength and microstructural characteristics of mine backfills containing fly ash and desulfurized gypsum. Minerals 2021;11(4):409.